

1 UNIVERSITY OF OKLAHOMA
2 GRADUATE COLLEGE
3 HOMER L. DODGE DEPARTMENT OF PHYSICS AND ASTRONOMY

4 THE MUON ANOMALOUS MAGNETIC MOMENT:
5 A PROBE FOR THE STANDARD MODEL AND BEYOND

6 A REPORT
7 SUBMITTED TO THE GRADUATE FACULTY
8 in partial fulfillment of the requirements for the
9 SPECIALIST'S EXAMINATION

10 By
11 OTHMANE RIFKI
12 Norman, Oklahoma
13 2014

14
15

THE MUON ANOMALOUS MAGNETIC MOMENT:
A PROBE FOR THE STANDARD MODEL AND BEYOND

16
17
18

A REPORT APPROVED FOR THE
HOMER L. DODGE DEPARTMENT OF PHYSICS AND
ASTRONOMY

19

BY

20

21 Table of Contents

22	List of Tables	iv
23	List of Figures	v
24	Abstract	vi
25	1 Introduction	1
26	2 The Muon Properties	6
27	2.1 Obtaining Polarized Muons	7
28	2.2 Parity Violation	8
29	2.3 Relativistic Muons in a Magnetic Field	12
30	3 Brookhaven $g - 2$ Experiment: E821	14
31	3.1 Historical Background	14
32	3.2 Description of the Experimental Method	15
33	3.3 Measurement of the Anomalous Angular Frequency ω_a	18
34	3.4 Measurement of the Magnetic Field B	23
35	3.5 Corrections and Systematic Errors	25
36	3.6 Summary of Results from E821	30
37	4 Future Fermilab $g - 2$ Experiment: E989	32
38	5 The Standard Model Evaluation of the Anomaly (a_μ)	35
39	5.1 Introduction	35
40	5.2 The QED Contribution to a_μ	37
41	5.3 The Weak Contribution to a_μ	39
42	5.4 The Hadronic Contribution to a_μ	40
43	5.5 The SM Value of a_μ	42
44	6 Conclusions and Prospects	44
45	References	46
46	A Spin Dynamics	47
47	B Muon Decay Rate	48
48	C Radiative Corrections	49

49 List of Tables

50	1	Systematic errors for ω_a	28
51	2	Systematic errors for ω_p	29
52	3	Results for the anomalous precession frequency ω_a	31
53	4	BNL E821 results of the anomaly a_μ	31
54	5	Comparison of systematic errors for ω_a between BNL and FNAL	35
55	6	Comparison of systematic errors for ω_p between BNL and FNAL	36

56 List of Figures

57	1	Pion decay	8
58	2	Muon decay	9
59	3	Decay electrons and asymmetry distributions in the muon rest frame . .	11
60	4	Injection chain in the muon $g - 2$ experiment	16
61	5	Muon spin precession in the storage ring	18
62	6	Electron detection in the storage ring.	19
63	7	Decay electrons and asymmetry distributions in the laboratory frame. .	21
64	8	Histogram of detected electrons	22
65	9	Feynman diagram of the lowest-order contribution	38
66	10	Feynman diagram of a weak contribution	39
67	11	Feynman diagram of some hadronic contributions	40
68	12	Different SM predictions of a_μ	43

69 Abstract

70 The muon is a spin- $\frac{1}{2}$ charged particle characterized by an intrinsic magnetic
71 moment with a *gyromagnetic ratio*, g , that is very close to 2. Its departure from
72 2, referred to as the magnetic moment anomaly $a_\mu = \frac{g-2}{2}$, has been determined
73 over the last decades to ever higher precisions in both experiment and theory. The
74 most recent experiment (E821) was performed at Brookhaven National Laboratory
75 and achieved a precision of 0.54 ppm, while the current theoretical evaluation
76 stands at a precision of 0.39 ppm. However, the experimental value is higher
77 than the predicted value by more than 3 standard deviations which suggests the
78 possibility of new physics. A new experiment (E989) is being built at Fermi
79 National Laboratory to investigate the discrepancy by reducing the experimental
80 error to 0.14 ppm. In parallel, theory groups are working to reduce the error in a_μ
81 to match the projected experimental precision. A confirmation of the difference
82 between experiment and theory will have an impact on new physics models at
83 the TeV scale. The goal of this review is to describe the E821 measurement of
84 a_μ , the improvements implemented in E989, the current theoretical status in the
85 computation of a_μ , and the new physics implications.

86 *The closer you look the more there is to see.*

87 Friedrich Jegerlehner, *The Anomalous Magnetic Moment of the Muon* [1].

88 **1 Introduction**

89 The study of elementary particles and their interactions led to a representative
90 mathematical formulation known as the *Standard Model* (SM) of particle physics.
91 When subjected to experimental tests, the SM successfully describes three of
92 the four fundamental forces: electromagnetic, weak, and strong interactions. On
93 the other hand, the SM is not believed to be complete since it fails to explain a
94 number of problems that are still facing today's physics community. First, the
95 SM does not incorporate the fourth fundamental force of gravity. Moreover, It
96 does not provide insight on the nature of the “invisible” matter that is holding
97 galaxies together, which constitutes $\sim 26\%$ of the energy density of the universe
98 and is known as *Dark Matter*. A few other examples are the different masses and
99 mixing of the 12 leptons known as the *flavor problem*, and the predominance of
100 matter over antimatter. In order to solve these problems, searches for physics
101 not incorporated in the SM have been pursued in both experiment and theory.
102 Any sign of significant discrepancy between experiment and theory is taken very
103 seriously since it might lead to new insights that can reveal what is missing in
104 our current view of the universe. Some experiments have looked for answers to
105 SM problems by studying high energy interactions as is pursued at the Large
106 Hadron Collider at CERN, in the hope of observing some new particles. This

107 led to the discovery of the Higgs boson in 2012, a central piece of the SM. Other
 108 experiments have performed detailed studies of known particles by measuring their
 109 properties to very high precisions and comparing them to theoretical calculations
 110 to both check the models and look for discrepancies. The subject of this current
 111 review is an important illustration of the latter scenario where precision tests
 112 of the intrinsic property of a spinning charged elementary particle known as the
 113 *magnetic moment* will be examined by comparing experiment to theory.

114 The possible elementary charged particles that can be used to measure the
 115 magnetic moment are the three spin $\frac{1}{2}$ leptons: the electron e , the muon μ , and
 116 the tau τ . While these particles have the same charge and spin, they have very
 117 different masses which are given by¹ $m_e = 0.511 \text{ MeV}/c^2$, $m_\mu = 105.658 \text{ MeV}/c^2$,
 118 and $m_\tau = 1776.82 \text{ MeV}/c^2$. The difference in masses alters the lifetimes and
 119 decay modes of each particle. The electron is the lowest mass charged lepton
 120 and thus is stable. The muon lifetime is $\tau_\mu = 2.197 \times 10^{-6}$ seconds and it decays
 121 almost 100% to an electron and two neutrinos ($e\nu_\mu\bar{\nu}_e$). Taus have a much shorter
 122 lifetime $\tau_\tau = 2.906 \times 10^{-13}$ seconds and a diversified decay pattern where 65%
 123 go into hadronic states (states that contain quark-antiquark pair particles such
 124 as pions) and the remainder go into leptonic states (the two possible states are
 125 muons and two neutrinos or electrons and two neutrinos) [2]. Because of its very
 126 short lifetime, the study of the tau's magnetic moment is difficult, leaving the
 127 electron and the muon as the appropriate candidates. While the electron is the
 128 most precisely studied lepton, effects in the magnetic moment sensitive to physics

¹The unit of mass is given in MeV/c^2 according to the relation $E = mc^2$ with the energy E given in units of MeV where $1 \text{ MeV} = 1.6 \times 10^{-13} \text{ J}$.

beyond the SM scale with powers of m_ℓ^2 [3]. For this reason, muons are more appropriate for the study of the magnetic moment to search for new physics.

The magnetic moment arises from the electric charge and the current of an elementary particle with spin. For instance, a classical calculation of a particle with mass m , and charge q , moving in a circular orbit of radius r , with velocity \vec{v} , shows that its magnetic moment $\vec{\mu}$ is related to its orbital angular momentum ($\vec{L} = m \vec{r} \times \vec{v}$) by the relation:

$$\vec{\mu} = \frac{q}{2mc} \vec{L} \quad (1)$$

(see Appendix A). In quantum mechanics, the magnetic moment is an intrinsic property of a particle with spin. Both the magnetic moment and the orbital angular momentum are promoted to operators in order to give the correct quantum mechanical representation. While Equation (1) is still valid in describing the orbital angular momentum \vec{L} , the spin magnetic moment requires a modification by a factor g that is very close to 2. The corrected equation is given by

$$\vec{\mu} = g \frac{q}{2mc} \vec{S}, \quad (2)$$

where g is called the *gyromagnetic ratio*, the Lande factor, or *g-factor* and q is the charge given in units of the fundamental charge e , where $q = -e$ for a lepton particle (negative muon) and $q = +e$ for a lepton antiparticle (positive muon). \vec{S} is the *spin operator*

$$\vec{S} = \frac{\hbar}{2} \vec{\sigma}, \quad (3)$$

where σ_i are the Pauli spin matrices. The result $g = 2$ was first obtained by Dirac in 1928 when he generalized the Schrödinger equation to incorporate special

148 relativity. With the development of the quantum mechanical description of
 149 electromagnetism known as quantum electrodynamics (QED), g was found to
 150 differ from 2 by an anomaly a_ℓ , known as the *magnetic moment anomaly*, or the
 151 *anomaly* for short, such that: $g_\ell = 2(1 + a_\ell)$. The anomaly is then

$$a_\ell = \frac{g_\ell - 2}{2}. \quad (4)$$

152 The $g - 2$ factor appeared! This is the title of all experiments that measure the
 153 magnetic moment of the muon and it is the focus of this review.

154 In addition to the quantum fluctuations of the electromagnetic field described
 155 by QED, quantum fluctuations due to heavier particles such as the weak gauge
 156 bosons (W^\pm and Z bosons) and hadrons (for example quark-antiquark pairs such
 157 as pions) also contribute to the anomaly. These effects are known as radiative
 158 corrections (RC) and are mainly dominated by QED as it will be discussed in
 159 Section 5. The anomaly scales as $\delta a_\ell \sim \frac{m_\ell^2}{M^2}$ where $M \gg m_\ell$ can represent the
 160 mass of a heavier SM particle, the mass of an unobserved heavy particle beyond
 161 the SM, or an energy range where the SM is no longer valid [3]. From this
 162 relation, we first see that a_μ is more sensitive to new effects than a_e by a factor of
 163 $(m_\mu/m_e)^2 \approx 4 \times 10^4$. On the other hand, heavier states (large M) have smaller
 164 effects ($\sim 1/M^2$) which places the determination of $g - 2$ as a good probe for
 165 interactions with energies at the TeV scale. The LHC is currently probing the
 166 TeV energy scale, so $g - 2$ will complement and guide the LHC searches and may
 167 even be more sensitive to new physics that is not accessible to the LHC.

168 The importance of $g - 2$ is in the fact that it can be precisely measured, as

will be discussed in Section 3, and it can be precisely calculated based on all RC of the SM as it will be discussed in Section 5. On the experimental side, the most recent experiment is the Brookhaven National Laboratory (BNL) E821 $g-2$ experiment that concluded its run in 2001, with a final reported result of [4]:

$$a_{\mu}^{\text{E821}} = (116\,592\,08.0 \pm 6.3) \times 10^{-10} \text{ (0.54 ppm) [4]}, \quad (5)$$

where ppm refers to the precision in parts per million given by the ratio of the total error to the value as σ_X/X . The anomaly has been evaluated by different groups. One of its recent calculations is

$$a_{\mu}^{\text{SM}} = (116\,591\,82.8 \pm 4.5) \times 10^{-10} \text{ (0.39 ppm) [5]}, \quad (6)$$

which gives a difference of

$$\Delta a_{\mu}(\text{E821} - \text{SM}) = (25.2 \pm 7.7) \times 10^{-10}. \quad (7)$$

The difference Δa_{μ} between the measurement and the prediction is 3.3 standard deviations with the measurement having the higher value. In particle physics, a three standard deviation effect “ 3σ ” means that the probability of the measurement to randomly fluctuate from the predicted value by 3σ is equivalent to the probability of obtaining a value on a Gaussian distribution that is at least 3 standard deviations away from the expected mean. This corresponds to a probability of 1.35×10^{-3} (on average 1 out of every 740 measurements). In order to be confident that the difference is not just a statistical fluctuation, a difference of five standard deviations “ 5σ ” is required, which implies that the probability of such variation is 3×10^{-7} (on average 1 out of every 3.5 million measurements).

187 An independent experiment is designed to reduce the error in Equation (5) to
 188 $\sim 1.6 \times 10^{-10}$ giving a precision of 0.14 ppm with a four-fold improvement over
 189 the BNL result [4]. Assuming that a similar value for the anomaly is obtained and
 190 the theoretical calculation is exactly the same, the new deviation is 5.3σ , which
 191 will confirm the discrepancy. This new experiment is currently being built at
 192 Fermi National Laboratory (FNAL) under the name E989 Muon $g - 2$ Experiment.
 193 An error improvement in the measurement of $g - 2$ implies that the error in the
 194 calculated prediction should also be improved to the same level. In the event
 195 that E989 confirms this discrepancy, severe constraints will be imposed on new
 196 theoretical models such as supersymmetry², extra dimensions³, or a dark matter
 197 particle, in order to account for the difference between experiment and theory.

198 This review will describe the experimental technique used to measure the
 199 anomaly and present the status of the theoretical calculations. It will also address
 200 the future improvements in both areas and conclude with new physics possibilities.

201 **2 The Muon Properties**

202 The muon anomaly can be measured to ppm precision by studying the behavior
 203 of the spin magnetic moment of muons in circular orbits subjected to a uniform
 204 magnetic field. In this section, the key ideas that permit the measurement will be
 205 introduced to lead up to a discussion of the BNL experiment in the next section.

²Supersymmetry (SUSY) theory postulates that a space-time symmetry exists between the two classes of the SM elementary particles: fermions and bosons. It incorporates the four fundamental forces and predicts energy interactions beyond the weak scale. However, experimental evidence has yet to support the theory.

³Extra dimension models postulate the existence of dimensions other than the three spatial dimensions and the temporal dimension.

2.1 Obtaining Polarized Muons

Muons are obtained from pions that are acquired from sending a high intensity beam of protons into a target material that has the property of being resistant to high stresses, nickel for example. The decay of positive and negative pions produces positive and negative muons according to

$$\begin{aligned}\pi^+ &\rightarrow \mu^+ + \nu_\mu, \\ \pi^- &\rightarrow \mu^- + \bar{\nu}_\mu.\end{aligned}\tag{8}$$

The spin orientation, called *polarization*, of the decayed muon is well determined for the cases of positive and negative pions. This can be seen by introducing the concepts of *helicity*, *parity transformation*, and *charge conjugation*. Helicity is defined as the projection of spin \vec{S} along the momentum direction $\hat{p} = \vec{p}/|\vec{p}|$ such that $h = \vec{S} \cdot \hat{p}$. For a spin- $\frac{1}{2}$ particle, it is right-handed when $h = +1/2$ (spin and momentum parallel) and left-handed when $h = -1/2$ (spin and momentum anti-parallel). Parity, represented by the operator P , creates the mirror image of a physical process. For example, for a vector \vec{x} , $P|\vec{x}\rangle = -|\vec{x}\rangle$. Charge conjugation, represented by the operator C , refers to the conversion of a particle to its antiparticle by changing the sign of all its quantum numbers (electric charge, lepton number, baryon number, and flavor charges such as strangeness).

By starting from a spin zero pion and a right-handed antineutrino, the possible transformations are C , P , or both CP as shown in Figure 1. Experimental evidence shows that neutrinos can only be left-handed and antineutrinos can only be right-handed. For this reason, the only possible process is the one obtained

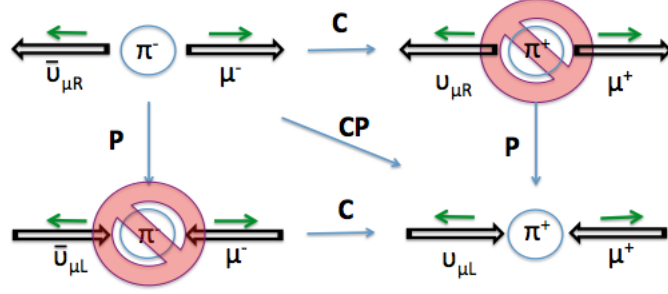


Figure 1: An illustration of the possible decays of a pion. The black arrow represents the spin vector and the green arrow represents the momentum orientation.

by a CP transformation, which makes a negative pion produce a right-handed negative muon ($h = +1/2$), and a positive pion produce a left-handed positive muon ($h = -1/2$).

2.2 Parity Violation

While parity is a conserved quantity in electromagnetic and strong interactions, it is not conserved in the weak interactions. In fact, the muon weak decays

$$\begin{aligned}\mu^- &\rightarrow e^- + \bar{\nu}_e + \nu_\mu, \\ \mu^+ &\rightarrow e^+ + \nu_e + \bar{\nu}_\mu\end{aligned}\tag{9}$$

are parity violating events, which means that the emitted electrons⁴ have a favored direction of emission. Because of parity violation in weak processes, a correlation exists between the momentum direction of the decaying electron and the spin orientation of the muon. In other words, there is a preferred direction for the decay of the electron for each spin orientation of the muon. For an illustration of

⁴Unless specified, electron refers to both the electron and its antiparticle, the positron.

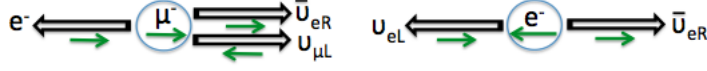


Figure 2: In the laboratory frame, the muon spin and momentum are parallel and directed to the right. Both decays are in the MRF and show the more likely electron direction. The left decay shows an electron having the maximum possible energy $E_{e,\max} \sim (m_\mu c^2)/2 = 53 \text{ MeV}$. The right decay shows an electron emitted at rest with its spin antiparallel to its laboratory momentum.

237 this correlation, the negative muon decay is considered in the two limiting cases of
 238 Figure 2 in the muon rest frame (MRF). Note that the muon momentum and spin
 239 are parallel and directed to the right in the laboratory frame to better understand
 240 the spin and momentum orientations of the right figure.

241 If the electron has the maximum possible energy in the MRF, the two neutrinos
 242 will be emitted back-to-back to the electron with the latter carrying approximately
 243 half of the rest mass energy of the muon in order to conserve momentum, $E_{e,\max} \approx$
 244 $(m_\mu c^2)/2 = 53 \text{ MeV}$ ⁵. Parity violation favors the electron to be emitted left-
 245 handed which implies that its momentum will be anti-parallel to the muon spin
 246 as shown in the left figure. In the case of a zero momentum electron in the MRF,
 247 the neutrino and antineutrino will be emitted antiparallel to each other with their
 248 spins parallel. Since the electron has a preferred spin direction antiparallel to
 249 the muon laboratory momentum, and the muon momentum and spin are parallel.

⁵More precisely, the conservation of energy leads to $E_{e,\max} = \frac{m_\mu^2 + m_e^2}{2m_\mu} c^2$. The above approximation holds when the value $\frac{m_e c^2}{E_{e,\max}} = 9.6 \times 10^{-3}$ is negligible.

250 The electron will be emitted parallel to the muon spin as shown on the right figure.
 251 These two examples show that by knowing the direction of the decay electron,
 252 the muon spin orientation can be inferred. This is the key idea of the muon $g - 2$
 253 measurement. By placing muons with the same polarization in a circular orbit
 254 with a uniform magnetic field, their spin component parallel to the momentum
 255 vector, longitudinal polarization, will change slightly with each orbit at a rate that
 256 is directly related to the anomaly $a_\ell = \frac{g_\ell - 2}{2}$. The change in the muon longitudinal
 257 polarization is determined by using the asymmetric angular distribution of the
 258 decay electrons. Formally, the differential decay probability for an electron to be
 259 emitted with a normalized energy $y = E/E_{e,max}$ at an angle θ with respect to the
 260 muon spin is given in the MRF with the approximation $E_e \gg m_e c^2$ by

$$dP^\pm \propto N(E_e) (1 \pm A(E_e) \cos \theta) dy d\Omega, \quad (10)$$

261 where the $(+)$ is for positive muons decay and the $(-)$ is for negative muons
 262 decay and $d\Omega$ is the solid angle. $N(E_e)$ is a normalization factor that represents
 263 the number of decay electrons per unit energy and $A(E_e)$ is the non-vanishing
 264 coefficient of $\cos \theta$ which represents the decay asymmetry factor that reflects the
 265 *parity violation*. The expressions of $N(E_e)$ and $A(E_e)$ are given by

$$N(E_e) = 2y^2 (3 - 2y) \quad \text{and} \quad A(E_e) = \frac{1 - 2y}{3 - 2y}. \quad (11)$$

266 These relations are derived in Appendix B.

267 A few remarks related to equations 10 and 11 are in order. First, the number
 268 of decay electrons and asymmetry reach their highest values in the MRF when
 269 the energy of the emitted electron is maximum ($y = 1$) as shown in Figure 3.

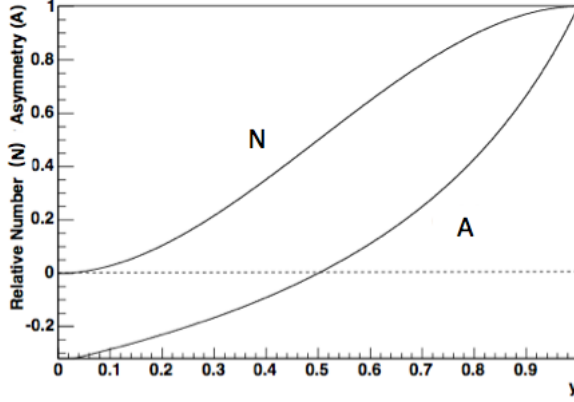


Figure 3: The number of decay electrons and the asymmetry distributions in the MRF as a function of the fractional energy $y = E/E_{e,max}$ [4].

Also, the asymmetry changes sign at half the maximum energy ($y = \frac{1}{2}$) which means that the emitted electron will have a preferred handedness (or helicity) based on its energy. More importantly, the probability of emitting a specific number of electrons varies with the angle θ between the electron and the muon spin directions. To be precise, there are more high energy electrons (e^-) emitted when their momenta are anti-parallel to the muon (μ^-) spins than when they are parallel. By only selecting the highest energy electrons and counting their number, the spin direction of the muons can be inferred: when the number of electrons is maximum, the muon spin is anti-parallel to the emitted electron direction, and when the number is minimum, the muon spin is parallel to the emitted electron direction. A similar reasoning can be followed for high energy positrons (e^+) which will reach a maximum number when the positive muon (μ^+) spins are parallel to the emitted positrons. If the spin of the muons is allowed to precess, then the

283 number of high energy electrons will also precess at the same rate, allowing a
284 direct measurement of the precession frequency.

285 2.3 Relativistic Muons in a Magnetic Field

286 In classical electromagnetism, the effect of a uniform magnetic field on a bar
287 magnet is to exert a torque that will align the magnet with the magnetic field.
288 However, if the magnet is spinning, then conservation of angular momentum will
289 cause the bar magnet to precess around the magnetic field. Similarly, the muon
290 has an intrinsic spin and an intrinsic magnetic moment. The interaction of the
291 muon magnetic moment with the magnetic field will cause a precession of the
292 spin around the magnetic field. In fact, it is the expectation value of the spin
293 operator that precesses around the magnetic field at a constant frequency known
294 as *Larmor frequency*. This frequency describes the gyration of the spin and is
295 proportional to the magnetic field, thus the name of *gyromagnetic ratio*, g . An
296 additional kinematic effect of precession is introduced due to the acceleration
297 of the relativistic reference frame. This is the case for muons moving at high
298 velocities with a transverse acceleration. This precession is derived in Appendix
299 A and is referred to as *Thomas precession*.

300 If relativistic muons are constrained to a circular orbit by a uniform magnetic
301 field, as is the case in a *storage ring*⁶, their spins experience both Larmor and
302 Thomas precessions. The ensemble of these effects on the spin was worked out
303 by Bargmann, Michel and Telegdi in 1959 [6], in an equation known as the BMT

⁶A storage ring is a circular particle accelerator that maintains particles at the same energy for a long period of time

304 equation (see Appendix A)

$$\vec{\omega}_s = \frac{q}{m_\mu c} \left\{ \left(a_\mu + \frac{1}{\gamma} \right) \vec{B} - a_\mu \left(\frac{\gamma}{\gamma + 1} \right) (\vec{\beta} \cdot \vec{B}) \vec{\beta} + \left(a_\mu + \frac{1}{\gamma + 1} \right) \vec{E} \times \vec{\beta} \right\}, \quad (12)$$

305 where the velocity is $\vec{\beta} = \frac{\vec{v}}{c}$, the Lorentz factor is $\gamma = 1/\sqrt{1 - \beta^2}$, \vec{E} and \vec{B} are
 306 the electric and magnetic fields in the laboratory frame respectively. In addition,
 307 the muons also travel in a circular orbit with a frequency known as the *cyclotron*
 308 *frequency* (see Appendix A)

$$\vec{\omega}_c = \frac{q}{\gamma m_\mu c} \left\{ \vec{B} + \frac{\gamma^2}{\gamma^2 - 1} (\vec{E} \times \vec{\beta}) \right\}. \quad (13)$$

309 It is convenient to choose a reference frame which rotates with the velocity vector
 310 in order to keep the equations simple. In this case, the precession is given by the
 311 difference of angular frequencies $\vec{\omega}_a = \vec{\omega}_s - \vec{\omega}_c$,

$$\vec{\omega}_a = \frac{q}{m_\mu c} \left\{ a_\mu \vec{B} - a_\mu \left(\frac{\gamma}{\gamma + 1} \right) (\vec{\beta} \cdot \vec{B}) \vec{\beta} + \left(a_\mu - \frac{1}{\gamma^2 - 1} \right) \vec{E} \times \vec{\beta} \right\}. \quad (14)$$

312 If the second and third terms are made to vanish by a proper choice of muon
 313 momenta and applied electric and magnetic fields, then Equation (14) becomes

$$\vec{\omega}_a = a_\mu \frac{q}{m_\mu c} \vec{B}. \quad (15)$$

314 In this case, a nonzero a_μ leads to a precession of the muon spin relative to the
 315 cyclotron frequency. This is the central equation of the $g - 2$ experiment that will
 316 be discussed in the next section.

317 **3 Brookhaven $g - 2$ Experiment: E821**

318 **3.1 Historical Background**

319 The muon magnetic moment has been measured by three consecutive experi-
320 ments at CERN through the 1960's and 1970's, and a more recent experiment
321 at Brookhaven National Laboratory (BNL), E821. The last CERN experiment
322 developed a number of novel techniques to measure the anomaly. For instance,
323 it employed a storage ring with a transverse uniform magnetic field to extend
324 the muon's lifetime and cancel the second term in Equation (14) since in this
325 case $\vec{\beta} \cdot \vec{B} = 0$. The experiment chose a specific momentum according to the
326 relation $a_\mu - 1/(\gamma^2 - 1) = 0$ in Equation (14) known as the *magic momentum*,
327 which causes the spin oscillation to be independent of any applied electric fields.
328 This equation requires the knowledge of the anomaly, which is the quantity the
329 experiment is set to measure. However, the value of the anomaly has already
330 been measured to the first decimal places, which is enough to determine the
331 momentum to the desired precision. The goal of the CERN experiment, on the
332 other hand, was to measure the anomaly to a higher precision. An anomaly
333 value of $a_\mu \approx 1.166 \times 10^{-3}$ led to a Lorentz factor value of $\gamma_{\text{magic}} \approx 29.30$, and
334 thus the magic momentum is approximately 3.09 GeV in the CERN experiment.
335 At the magic momentum, electric quadrupoles⁷ were used to provide vertical
336 focusing of the beam. The combined results of the CERN run established a
337 7.3 ppm precision that was consistent with the standard model prediction. The

⁷An electric quadrupole is a system composed of two pairs of oppositely polarized poles placed antiparallel to each other.

338 new measurement techniques developed at CERN were used at Brookhaven with
 339 some notable improvements such as the higher intensity of the primary proton
 340 beam from the proton storage ring; the direct injection of muons into the storage
 341 ring instead of pions; the use of kickers to place muons on the correct orbits;
 342 the high field uniformity; and the use of Nuclear Magnetic Resonance probes to
 343 map the magnetic field distribution. The E821 experiment resulted in a 14-fold
 344 improvement over the CERN experiment where it performed four positive muon
 345 runs and one negative muon run which gave a combined precision of 0.54 ppm.
 346 In this section, a description of the E821 experiment and the summary of its
 347 measurements is given.

348 **3.2 Description of the Experimental Method**

349 At BNL, 24 GeV protons are extracted from the proton storage ring AGS (Al-
 350 ternating Gradient Synchrotron) and directed towards a nickel target to generate
 351 pions. The pions subsequently decay to muons which pass through selectors that
 352 maximize the number of longitudinally polarized muons at the magic momentum
 353 of 3.094 GeV/c. These muons are injected into the storage ring via a tangent 1.7
 354 meters long superconducting inflector magnet that provides a 1.5 Tesla vertical
 355 field. The field cancels the main storage ring field, allowing the muons to pass
 356 almost undeflected into the ring. The muon storage ring has a toroid-shaped
 357 structure with a diameter of 14 meters, a beam pipe with a diameter of 90 mm,
 358 and a uniform field of 1.45 Tesla. This magnetic field is provided by dipole

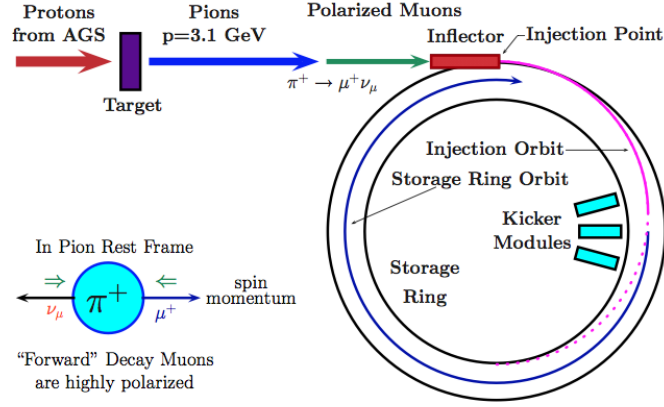


Figure 4: The chain of injection and storage of positive muons in the muon $g-2$ ring at BNL. The “forward” muons refer to muons decaying in the same direction as the laboratory momenta. In this situation, positive muons have their spins anti-parallel to their momenta [3].

359 magnets⁸ that maintain muons in the desired trajectories. However, when the
 360 muons are first injected, their trajectories are offset from the storage ring orbit.
 361 Pulsed kicker magnets are placed at a specific location in the ring, close to the
 362 inflector exit in order to apply a small magnetic field, a “kick,” to adjust the orbit
 363 by approximately 10 mrad on each injection. Figure 4 shows the complete chain
 364 of the muon $g-2$ experiment at BNL for positive muons.

365 Beam focusing is also needed to constrain the muons within the desired
 366 trajectories. Since electric fields do not affect the spin precession, electrostatic
 367 quadrupoles are used to continuously focus and defocus the beam in the vertical
 368 and the horizontal directions in order to precisely control the beam.

369 Muons will travel around the ring at the cyclotron angular frequency described

⁸A dipole magnet is a configuration of two opposite pole magnets in the vertical plane of the ring which provide a transverse magnetic field.

by Equation (13), which has a value of approximately 149 ns, and their spin will interact with the magnetic field resulting in a precession with the angular frequency ω_s given by Equation (14). However, the electric field \vec{E} is negligible ($E \approx 0$) and the uniform magnetic field is transverse ($\vec{\beta} \cdot \vec{B} = 0$), so the anomalous precession frequency, $\vec{\omega}_a$, is given by Equation (15) to the first order. Its magnitude is

$$\omega_a = a_\mu \frac{eB}{m_\mu c} \quad (16)$$

If $g = 2$, then this relative precession ω_a will be zero, which implies that the muon spin is precessing at the same frequency as the cyclotron frequency. On the other hand, if $g \neq 2$, the muon spin will precess at a different rate than the cyclotron frequency, leading the muon spin axis to change by 12 degrees⁹ after each rotation for a constant momentum. Figure 5 illustrates this change by showing the momentum vector and the projection of the spin vector in the horizontal plane of the storage ring.

In order to determine the anomaly $a_\mu = \frac{g_\mu - 2}{2}$, three quantities need to be determined accurately: ω_a , B , and the muon mass m_μ . The muon mass was determined indirectly by an independent experiment on muonium, the bound state of μ^+e^- [7]. The next two subsections describe the measurement of ω_a and the magnetic field B .

⁹The angular change of spin relative to momentum after one revolution around the ring is $\theta_a = \omega_a T_c$. For $a_\mu \approx 1.166 \times 10^{-3}$, $m_\mu = 105.7 \text{ Mev}/c^2$, $e = 1.6 \times 10^{-19} \text{ C}$, and $B = 1.45 \text{ T}$, $\omega_a \approx 1.45 \times 10^6 \text{ Hz}$ and $T_c \approx 149 \text{ ns}$, the result using Gaussian units is $\theta_a \approx 12^\circ$.

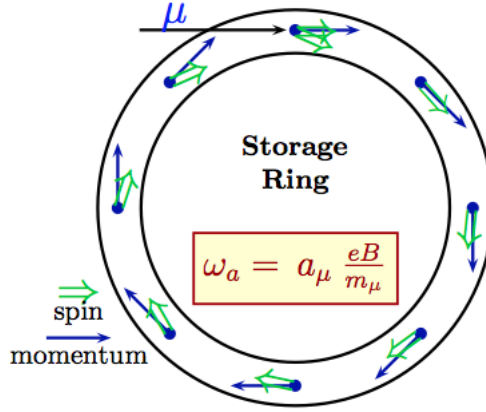


Figure 5: Illustration of the spin precession in the storage ring plane relative to a constant momentum (not to scale). The precession amounts to ~ 12 degrees per orbit [3].

3.3 Measurement of the Anomalous Angular Frequency ω_a

As a result of the muons' high momentum (~ 3.1 GeV), their lifetime is extended from $2.197 \mu s$ at rest to $64.435 \mu s$ in the ring. The muons circle the ring many times before they decay into an electron and two neutrinos given by Equation (9). As discussed in Section 2.2, the electron has a preferred emission direction in the muon rest frame that depends on the orientation of the muon spin as given by Equation (10). For example, a positron has a higher probability to be emitted parallel to the muon spin (see Figure 6).

If all decay electrons were detected, the number observed will decay exponentially as $\exp(\frac{-t}{\gamma\tau_\mu})$. Since the interest is in the precession frequency, a choice of a cut on a laboratory observable that directly depends on this frequency is required. A reasonable choice will permit the selection of a subset of the decay electrons in such a way that their number oscillates at the desired frequency ω_a .

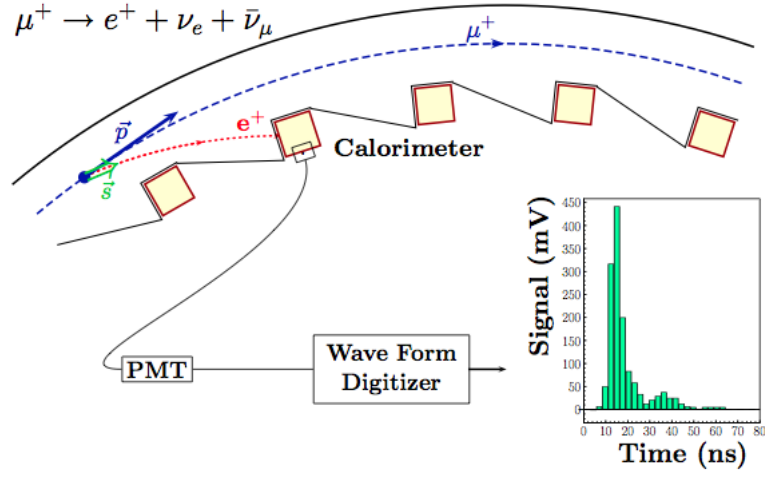


Figure 6: A positive muon in the storage ring emits a positron almost parallel to the muon spin (green arrow). The electron is subjected to the same dipole magnetic field which produces a larger deflection leading the positron to interact with the calorimeter scintillator. The light is detected by a Photomultiplier Tube (PMT) generating a signal that is digitized by a Wave Form Digitizer [3].

400 At the magic momentum $p_\mu \approx 3.09$ GeV/c, the direction of the electrons cannot
 401 be chosen as a cut since most decay electrons are nearly parallel to the muon
 402 momentum direction, regardless of their decay orientation in the muon rest frame.
 403 Instead, a more practical cut can be applied on the electron's laboratory energy.
 404 For instance, if only electrons with the highest possible energy are selected, they
 405 will represent positrons that decayed nearly parallel to the muon laboratory mo-
 406 mentum with maximum muon rest frame energy. The number of these positrons
 407 is larger when they are emitted parallel to the muon spin as opposed to when they
 408 are antiparallel. So the number of positrons detected will be maximum when the
 409 spin is aligned with the decay positron momentum, and will be minimum when
 410 the spin is opposite. It becomes clear that the detected electrons will oscillate
 411 with the frequency of the muon spin oscillation ω_a .

412 In practice, the minimum energy threshold is selected to maximize the *statistical*
 413 *figure-of-merit* (FOM), NA^2 , in order to minimize the statistical uncertainty. On
 414 the left of Figure 7, NA^2 is largest for electrons with $E_{th} \approx 2.6$ GeV ($y \approx .85$).
 415 However, the interest is in electrons above an energy threshold. By integrating
 416 the quantities N , A , and NA^2 for a single electron threshold as a function of the
 417 energy threshold, NA^2 is maximized at $E_{th} \approx 1.8$ GeV as shown on the right of
 418 Figure 7.

419 With the the assumption that the spin precession vector is independent of
 420 time, the angle between the spin component in the orbit plane and the muon
 421 momentum is $\omega_a t + \phi$, where ϕ is a constant phase. At time t , the number of

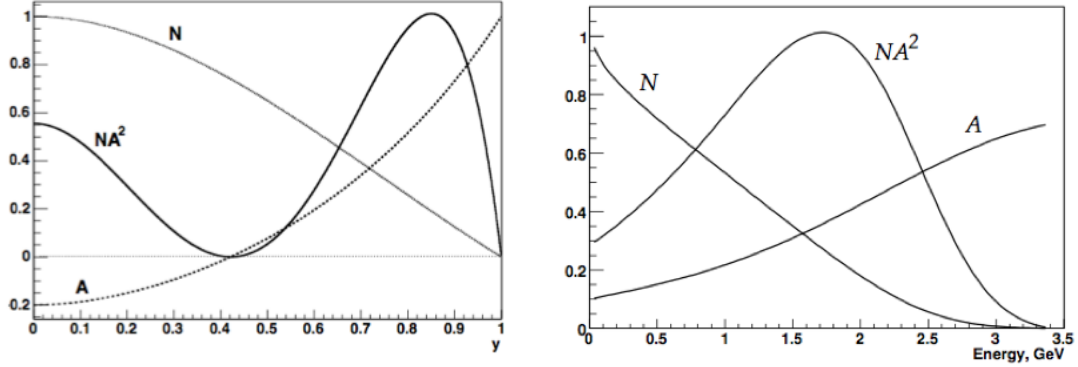


Figure 7: The equivalent of Figure 3 boosted to the laboratory frame.

Left: N , A , and NA^2 as a function of the fractional energy $y = E/E_{e,max}$ where $E_{e,max} \approx 3.098$ GeV. Right: Integrated N , A , and NA^2 as a function of the threshold energy [4].

decay positrons $N(t)$ with energy larger than the threshold energy E_{th} is

$$N(t, E_{th}) = N_0(E_{th}) \exp\left(\frac{-t}{\gamma\tau_\mu}\right) [1 + A(E_{th}) \sin(\omega_a t + \phi(E_{th}))], \quad (17)$$

where N_0 is a normalization factor and A is the asymmetry factor for positrons of energy greater than E_{th} . Figure 8 shows the arrival-time spectrum of the final E821 data run for 2001. As discussed earlier, the spectrum follows an exponential decay of the muons modulated by the $g - 2$ dependent angular frequency. By fitting this time distribution to the five-parameter function of Equation (17), the angular frequency ω_a is determined.

The electron detection is made via 24 symmetrically distributed calorimeters inside of the ring as shown in Figure 6. The goal of the calorimeters is to determine the electrons' energy and arrival time. The calorimeters are designed to detect the high energy electrons where 65 percent of the electrons with energy higher than

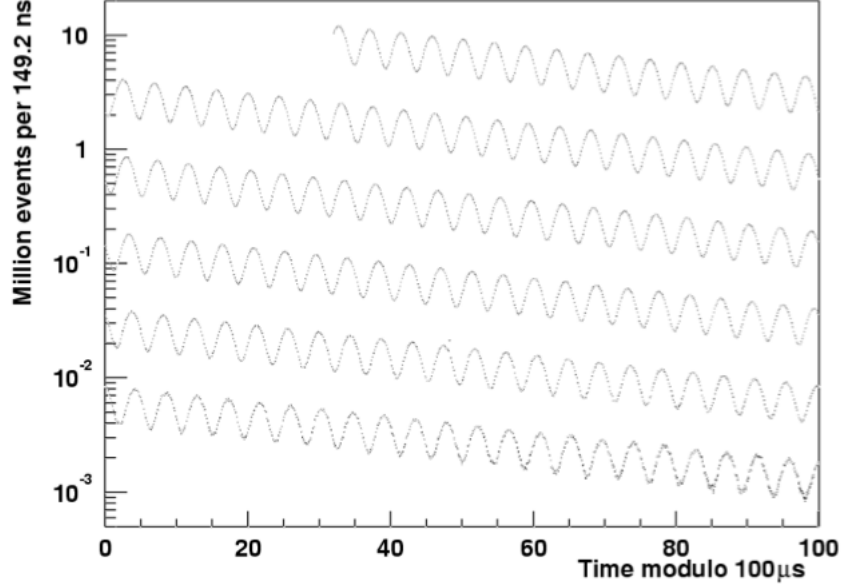


Figure 8: Histogram of the 3.6 billion detected electrons above 1.8 GeV as a function of time, modulo $100 \mu s$, for the 2001 data set [4].

433 1.8 GeV are intercepted [4]. Each calorimeter is made out of plastic-scintillator¹⁰
434 material (52% lead alloy, 38% scintillating fiber, and 10% epoxy) read out by
435 photomultiplier tubes¹¹ (PMTs). The decaying electrons have both tangential
436 and radial momentum components. However, the radial component is quite small,
437 which permits the extrapolation of the electron's trajectory from the calorimeter
438 to the central muon orbit, allowing a measurement of the decay position and
439 vertical angle as shown in Figure 6. The muon position information is particularly
440 important in characterizing the magnetic field felt by the muon at that specific
441 location. Finally, a Wave Form Digitizer (WFD) captures raw analog PMT signals

¹⁰A plastic-scintillator causes the particle to deposit energy when it passes through. The scintillator re-emits the absorbed energy in the form of light.

¹¹Photomultiplier tubes are light detectors that operate via the photoelectric effect where photons, upon hitting a photocathode, generates a cascade of electrons that can be read by a Wave Form Digitizer.

442 and digitizes them for further processing with the advantage of maintaining high
443 resolution measurements. An example of a WFD output is shown in Figure 6.

444 3.4 Measurement of the Magnetic Field B

445 The magnetic field B is weighted by the stored muons distribution and averaged
446 over the running time. It can be expressed as an integral of the product of the
447 muon distribution multiplied by the magnetic field distribution over the storage
448 region leading to a coupling of the moments of the muon distribution to the
449 respective multipoles of the magnetic field. In order to determine the weighted
450 magnetic field B to sub-ppm precision, either the moments and multipoles of
451 the muon and magnetic field distributions should be known extremely well, or a
452 particularly uniform magnetic field and a circular beam aperture is required so
453 that the leading term dominate the multipole expansion of the magnetic field. The
454 latter option was selected where *Nuclear Magnetic Resonance* (NMR) permitted
455 the determination of the magnetic field to the tens of ppb. In this experiment,
456 NMR uses protons in a water sample placed in the dipole magnetic field, and
457 exposed to a $\frac{\pi}{2}$ radio-frequency (RF) pulse which rotates the net magnetization of
458 the protons¹². A pickup coil placed in the transverse direction registers the induced
459 signal that exponentially decays with an oscillation as the protons' magnetization
460 regains its equilibrium position. This process is known as *Free Induction Decay*,
461 which has a frequency sensitive to the the local magnetic field value. The NMR

¹²A radio-frequency pulse is a pulse in the range from 3 KHz to 300 GHz that excites a large frequency band resulting in the appearance of a time-dependent magnetic field which can rotate the magnetization vector of the protons.

462 procedure allows the determination of the magnetic field at thousands of points
 463 around the ring which permits the mapping and monitoring of the field during
 464 data taking. A calibration method is used to express the Larmor spin frequency
 465 of a proton in a water sample in terms of the Larmor spin frequency of a free
 466 proton ω_p . The latter frequency, ω_p , is related to the magnetic moment of the
 467 free proton μ_p and the magnetic field B by ¹³

$$B = \frac{\hbar\omega_p}{2\mu_p}. \quad (18)$$

468 According to the last equation, this weighted magnetic field can be referred to as
 469 ω_p . By writing Equation (2) in the form $\frac{q}{mc} = \frac{2\mu_\mu}{1+a_\mu}$ and using Equation (16)
 470 and Equation (18), the anomaly can be written in terms of dimensionless ratios,

$$a_\mu = \frac{\mathcal{R}}{\lambda - \mathcal{R}}, \quad (19)$$

471 where $\lambda \equiv \frac{\mu_\mu}{\mu_p}$ and $\mathcal{R} \equiv \frac{\omega_a}{\omega_p}$. The muon-to-proton magnetic moment ratio, λ ,
 472 embodies in it both the muon and the proton masses since $\frac{\mu_\mu}{\mu_p} = \frac{g_\mu m_p}{g_p m_\mu}$. Its
 473 value is determined through a precision measurement of the Zeeman ground state
 474 hyperfine transitions in muonium (μ^+e^-) by E1054 LAMPF at Los Alamos [7],

$$\lambda_+ = \frac{\mu_{\mu^+}}{\mu_p} = 3.183\,345\,137\,(85).$$

475 Note that this result has a precision of ~ 27 ppb which could not be obtained by
 476 mass measurements. The use of λ_+ to determine a_{μ^-} implies CPT invariance¹⁴.

¹³The Larmor frequency of a free proton is $\omega_p = \gamma_p B$, where γ_p is the free proton gyromagnetic moment ratio given by Equation (2) such that $\vec{\mu}_p = \gamma_p \vec{S}$. These relations give the result in Equation (18).

¹⁴CPT invariance implies that the product of the three discrete transformations C, P, and T taken in any order is a symmetry of theories like the SM. It guarantees that particles and antiparticles have the same masses and lifetimes.

477 In other words, the relations $a_{\mu^-} = a_{\mu^+}$ and $\lambda_+ = \lambda_-$ must be valid. In fact, the
 478 measurement of ω_a for positive and negative muons provides a CPT test where

$$\Delta\mathcal{R} = \mathcal{R}_{\mu^-} - \mathcal{R}_{\mu^+} = (3.6 \pm 3.7) \times 10^{-9}. \quad (20)$$

479 3.5 Corrections and Systematic Errors

480 The method described so far presents an ideal scenario. However, there are
 481 additional effects that affect the measurements, the most important of which are
 482 related to the beam dynamics leading to a displacement of the beam trajectory
 483 and the determination of the magnetic field at a location offset from the orbit of
 484 the muons. While the dipole magnetic field insures the bending of the muon beam,
 485 the vertical focusing is done via electric quadrupoles. These quadrupoles set an
 486 electric field gradient that causes the beam to oscillate around its equilibrium in
 487 the plane transverse to the beam. This type of oscillation is known as the *betatron*
 488 *oscillation* and it satisfies the harmonic oscillator equations

$$\begin{aligned} \ddot{x} + \omega_x^2 x &= 0, \\ \ddot{y} + \omega_y^2 y &= 0, \end{aligned} \quad (21)$$

489 with the frequencies

$$\omega_x = \omega_c \sqrt{1-n}, \quad \omega_y = \omega_c \sqrt{n}, \quad (22)$$

490 where ω_c is the cyclotron frequency and n is the field index defined as

$$n = \frac{R_0}{\beta B_0} \frac{\partial E_y}{\partial y}, \quad (23)$$

491 with an orbit stability condition of $0 < n < 1$ and where R_0 is the equilibrium
 492 radius, B_0 is the dipole magnetic field, and β is the muon speed. Since the betatron

493 frequencies are smaller than the cyclotron frequency, this type of focusing is called
 494 *weak focusing*.

495 The betatron motion perturbs the muon trajectories affecting their momenta
 496 and directions. This implies that the assumptions $\vec{\beta} \cdot \vec{B} = 0$ and $a_\mu - 1/(\gamma^2 - 1) =$
 497 0 ($E \approx 0$) are no longer valid. These effects should be taken into account in
 498 determining the anomalous frequency ω_a as given by Equation (15). The correction
 499 for the momentum direction to satisfy $\vec{\beta} \cdot \vec{B} = 0$ is called the *Pitch Correction*.
 500 Similarly, the momentum spread from the magic momentum requires a correction
 501 to the electric field referred to as the *Radial Electric Field Correction*. The
 502 combination of these two corrections are explicitly shown in column 4 of Table 3.

503 Next, the sources of systematic errors in ω_a are briefly defined with their
 504 numerical values listed in Table 1:

- 505 • Pileup: Two low-energy electrons that reach the detector at very close times
 506 can be interpreted as one high-energy electron.
- 507 • AGS background: Mis-steering the proton beam in the AGS might lead it
 508 to hit a part of the target that produces a higher flux of pions entering the
 509 storage ring when muons are injected.
- 510 • Lost muons: Small perturbations in the magnetic or electric fields may
 511 couple to betatron oscillations at their resonant frequency leading to a
 512 motion without bound until the muons are lost.
- 513 • Timing shifts and gain changes: A calibration pulse was sent in parallel to
 514 the beam data through the optical and electronic readout system to monitor

515 the time resolution of the detector and variations in the energy scale used.

516 • Fitting/Binning: The electron decay spectra was sorted into discrete energy
517 bins and fitted to a multi-parameter fitting function for different data subsets
518 which introduced errors related to the corrections applied to the spectra
519 and the experimental conditions.

520 • Coherent Betatron Oscillation (CBO): Mismatch between the inflector and
521 storage ring apertures at the injection point causes the beam to alternatively
522 widen and narrow as it circulates around the ring.

523 The systematic uncertainties in the magnetic field measurement are due to
524 effects related to the determination of the precession frequency of protons in a
525 water sample placed in a trolley probe that is offset from the orbit of the muons.
526 The positioning of the trolley permits measurements of the magnetic field during
527 data taking at multiple locations around the ring. However, the magnetic field
528 at the trolley's position might vary from the field that muons experience. In
529 addition, the desired quantity is the free proton precession, but the measured
530 quantity is the proton's precession in water. For these reasons, uncertainties are
531 introduced in the processes of calibration and interpolation. Table 2 summarizes
532 the numerical values of the errors in ω_p for three running periods.

533 The electric dipole moment (EDM) of the muons should also be mentioned for
534 completeness of the discussion. Just as the magnetic moment originates from the
535 current of the spinning charged lepton and interacts with the magnetic field, the
536 EDM is due to the electric charge of the spinning lepton and it interacts with the

Table 1: Systematic errors for ω_a for the three high-statistics running periods. † In the 2001 run, the AGS background, timing shifts, E field and pitch correction, binning and fitting procedure have a total systematic error of 0.11ppm.

Years	1999	2000	2001
	(ppm)	(ppm)	(ppm)
Pileup	0.13	0.13	0.08
AGS background	0.10	0.01	†
Lost Muons	0.10	0.10	0.09
Timing Shifts	0.10	0.02	†
E-field and pitch	0.08	0.03	†
Fitting/Binning	0.07	0.06	†
CBO	0.05	0.21	0.07
Gain Changes	0.02	0.13	0.12
Total systematic error on ω_a	0.3	0.31	0.21

Table 2: Systematic errors for ω_p for the three high-statistics running periods. † After 1999, the inflector, which was damaged, was replaced making the disturbance of the inflector’s fringe field on the main storage ring field negligible.

Years	1999	2000	2001
	(ppm)	(ppm)	(ppm)
Absolute calibration of standard probe	0.05	0.05	0.05
Calibration of the trolley probes	0.20	0.15	0.09
Trolley measurements of B	0.10	0.10	0.05
Interpolation with fixed probes	0.15	0.10	0.07
Uncertainty from muon distribution	0.12	0.03	0.03
Inflector fringe field uncertainty	0.20	†	†
Others	0.15	0.10	0.10
Total systematic error on ω_p	0.4	0.24	0.17

537 electric field. The equivalent of Equation (2) for an EDM is

$$\vec{d} = \eta \frac{q}{2mc} \vec{S} \quad (24)$$

538 where d is the dimensionless constant equivalent to the g-factor. Equation (19)

539 assumes a zero muon EDM. For a non-zero muon EDM, the spin frequency is

$$\vec{\omega} = \vec{\omega}_a + \vec{\omega}_{EDM} = \vec{\omega}_a - \frac{q\eta}{2m} (\vec{\beta} \times \vec{B}) \quad (25)$$

540 However, the current experimental value for muons EDM is $d_\mu = (-0.1 \pm 0.9) \times$

541 $10^{-19} e \cdot \text{cm}$ [2], which is too small to affect the anomalous precession frequency ω_a .

542 3.6 Summary of Results from E821

543 E821 has conducted four positive muon runs (1997-2000) and one negative

544 muon run (2001) that are all reported in [4]. The results of the experiment for

545 the last three runs are displayed in Table 3 and Table 4.

546 The averaged value of the ratio $\mathcal{R} = \omega_a/\omega_p$ of Equation (19) evaluated in the

547 cases of negative and positive muons is

$$\mathcal{R}_\mu (\text{E821}) = 0.003\,707\,206\,4(20). \quad (26)$$

548 The anomalous magnetic moment is thus

$$a_\mu^{\text{E821}} = 11\,659\,208\,(5.4)_{\text{stat}}\,(3.3)_{\text{sys}}\,(6.3)_{\text{tot}} \times 10^{-10} \quad (0.54 \text{ ppm}) \quad (27)$$

549 This final measurement has a statistical uncertainty of 0.46 ppm and a systematic

550 uncertainty of 0.28 ppm which were added in quadrature to get a total uncertainty

551 of 0.54 ppm. In order to improve the statistical uncertainty to the same level as

Table 3: Results for the anomalous precession frequency ω_a including the relative electric field and pitch corrections shown in column 4 and the event-weighted magnetic field ω_p given with their uncertainties. The error on the average takes into account the correlated systematic uncertainties between different periods.

Years	Electrons	$\omega_a/(2\pi)$	E/pitch	$\omega_p/(2\pi)$	$\mathcal{R} = \omega_a/\omega_p$
	[millions]	[Hz]	[ppm]		
1999 (μ^+)	950	229 072.8(3)	0.81(8)	61 791 256(25)	0.003 707 204 1(51)
2000 (μ^+)	4000	229 074.11(16)	0.76(3)	61 791 595(15)	0.003 707 205 0(25)
2001 (μ^-)	3600	229 073.59(16)	0.77(6)	61 791 400(11)	0.003 707 208 3(26)
Average					0.003 707 206 3(20)

Table 4: BNL E821 results of the anomaly a_μ for the three high-statistics running periods.

Years	Polarity	$a_\mu \times 10^{10}$	Precision [ppm]
1999	μ^+	11 659 202(15)	1.3
2000	μ^+	11 659 204(9)	0.73
2001	μ^-	11 659 214(9)	0.72
Average		11 659 208.0(6.3)	0.54

the systematic uncertainty, an additional running period of 8 years is required. Alternatively, the experiment can use a higher intensity beam to produce more electrons, and thus more statistics. This is precisely what the new Fermilab experiment does.

4 Future Fermilab $g - 2$ Experiment: E989

The Fermilab experiment, E989, will measure the anomaly a_μ with an error of 1.6×10^{-10} leading to a fractional error of 0.14 ppm, where the level of the statistical and systematic uncertainties are both at the 0.10 ppm level. In order to achieve this goal, a collection of data that is twenty-one times larger than the E821 data collection is required, which scales to 1.8×10^{11} detected positrons with energy greater than 1.8 GeV, and arrival time greater than $30 \mu s$ after muon injection in the storage ring. Since the detected positron number is directly proportional to the protons on target, the Fermilab experiment will have to deliver 4×10^{20} protons. Indeed, it will be possible to reach these numbers by using the Fermilab beam complex which is expected to annually deliver 2.3×10^{20} 8 GeV protons on an Inconel¹⁵ core target. At this rate, the desired number of protons, and thus positrons, will be achieved in less than two years of running.

Fermilab will improve upon the methods and instrumentation used at BNL. For instance, the produced pion beam will pass through a bending magnet to select particles with a momentum of 3.1 GeV ($\pm 10 \%$), and subsequently traverse

¹⁵Inconel is an alloy, composed of a metal and other elements, specifically designed to withstand high beam stresses.

572 a decay line of over one kilometer, which results in a pure muon beam entering
 573 the storage ring. The muon storage ring will be filled at a repetition rate of 15
 574 Hz compared to 4.4 Hz at BNL, and the stored muon-per-proton ratio will also
 575 be increased by a factor of 5 to 10 times. The muons will enter the ring via a new
 576 superconducting inflector, characterized by a limited flux leakage onto the storage
 577 region and a larger horizontal beam aperture to allow a higher storage efficiency.
 578 The muon kicker will have an optimized pulse-forming network¹⁶ that will provide
 579 a pulse close to the beam width, as opposed to the E821 kicker which had a pulse
 580 width longer than the cyclotron period. At BNL, the injected muon beam was
 581 contaminated with pions which introduced a hadronic flash background. This
 582 background will be reduced by a factor of 20 in E989.

583 E989 will use the same muon storage ring as E821, which was relocated to Fermilab
 584 in the summer of 2013 in a new building characterized by mechanical stability
 585 and controlled temperature. These options were not available at BNL.

586 The new segmented calorimeters will use silicon Photomultipliers (SiPMs)
 587 to read signals from lead-fluoride crystal (PbF_2). The crystal has an improved
 588 energy resolution and a very fast Cherenkov signal¹⁷ response. When a photon
 589 strike a SiPM pixel, it generates an avalanche that is linearly combined with
 590 the other pixels that were hit to form the response. SiPMs are designed so that
 591 their number of pixels exceed the number of photons that are expected to strike

¹⁶A pulse-forming network is an electric circuit composed of capacitors that provide a square pulse with a flat top upon discharge.

¹⁷A Cherenkov signal is due to Cherenkov radiation which is an electromagnetic radiation produced when a particle travels through a dielectric material with a velocity greater than the phase velocity of light in that dielectric. While no particle travels faster than light in vacuum, the situation is different in a dielectric since $v_{\text{light}} = c/n$ with $n > 1$.

the device allowing a high photo-detection efficiency. The added benefit of using SiPMs is that they can be placed inside the storage ring at the back of the PbF₂ crystals without perturbing the field, as opposed to PMTs which require long lightguides.

Since momentum spread, betatron oscillations, and muon distribution introduced ppm level corrections in the anomalous precession at BNL, E989 introduces in-vacuum straw drift tubes¹⁸ as tracking detectors to better understand beam dynamics, limit pile up effects, and provide an independent validation of the systematic uncertainties analysis (for example, an independent momentum measurement). In addition, it will also be used to search for a permanent EDM. The electronics and data acquisition systems will be upgraded to handle the increased rate of data taking and to record all information related to the run for monitoring and the application of corrections in the analysis stage.

Last but not least, the storage ring magnetic field, and thus ω_p , will be measured with an uncertainty that is approximately 2.5 times smaller by placing critical NMR probes at strategic locations around the ring and shimming the magnetic field to achieve a high uniformity in addition to other incremental adjustments. Tables 5 and 6 compare the systematic uncertainties in ω_a and ω_p as obtained by BNL E821 and as planned for FNAL E989 experiments [8].

¹⁸A straw tube for high resolution position measurement is constructed with an anode wire centered within a cathode tube and maintained at a potential difference in a gas environment. When a charged particle passes through the tube, it ionizes the gas generating a signal for a particle “hit”.

Table 5: Comparison of systematic errors for ω_a between BNL E821 and FNAL E989.

Category	E821 (2001)	E989 Goal
	(ppm)	(ppm)
Pileup	0.08	0.04
Lost Muons	0.09	0.02
E-field and pitch	0.05	0.03
CBO	0.07	< 0.03
Gain Changes	0.12	0.02
Total systematic error on ω_a	0.18	0.07

5 The Standard Model Evaluation of the Anomaly (a_μ)

5.1 Introduction

The magnetic moment of the muon is described by Equation (2)

$$\vec{\mu} = g \frac{q}{2mc} \vec{S}, \quad g = 2(1 + a_\mu), \quad (28)$$

where $g = 2$ in the Dirac theory. Particles with $g = 2$ are referred to as Dirac particles. The anomaly a_μ is due to quantum fluctuations that couple the muon spin to virtual fields which leads to contributions that can be calculated in the SM theory. For instance, the three interactions that the SM describes are electromagnetic interactions by Quantum Electrodynamics (QED), hadronic strong interactions by Quantum Chromodynamics (QCD), and weak interactions by the Electro-Weak theory (EWT). In this language, the anomaly can be written

Table 6: Comparison of systematic errors for ω_p between BNL E821 and FNAL E989.

Category	E821 (2001) (ppm)	E989 Goal (ppm)
Absolute calibration of standard probe	0.05	0.035
Calibration of the trolley probes	0.09	0.03
Trolley measurements of B	0.05	0.03
Interpolation with fixed probes	0.07	0.03
Uncertainty from muon distribution	0.03	0.03
Time dependent external B fields	—	0.005
Others	0.10	0.03
Total systematic error on ω_p	0.17	0.070

621 as the sum of contributions from each theory as

$$a_{\mu}^{SM} = a_{\mu}^{\text{QED}} + a_{\mu}^{\text{Hadronic}} + a_{\mu}^{\text{EW}}. \quad (29)$$

622 The QED and weak contributions to the anomaly are well understood and
623 have been evaluated using perturbation theory to a high precision leading to
624 small errors, and thus permitting the comparison with experimental results. On
625 the other hand, the hadronic contribution limits the accuracy of the theoretical
626 prediction since these effects cannot be evaluated using perturbation methods
627 at low energies. For this reason, the hadronic contribution has to be evaluated
628 using experimental data via a dispersion relation, and thus leading to the highest
629 uncertainty in the prediction.

630 5.2 The QED Contribution to a_{μ}

631 Electromagnetic processes involve the interactions between charged particles
632 and the photon. In loose language, sometimes the muon will “recapture” the
633 photon it emitted and thus form a new “Dirac muon + photon” system. If the
634 magnetic moment of the muon is probed at that instant, it will be different than
635 2 since the configuration does not have just a Dirac muon. Similarly, there can be
636 more than one photon or even electron-positron pairs that form a new system,
637 and thus the contributions to g of Equation (28) can be expressed as a series
638 in the form: Dirac muon + {Dirac muon + photon} + {Dirac muon + several
639 photons} + {electron + positron}

640 Formally, the dominant contribution is that of the lowest-order (LO) QED

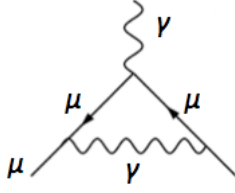


Figure 9: The lowest-order (Schwinger) contribution to the muon magnetic moment anomaly [10].

process that involves the exchange of a virtual photon and is represented by a one-loop diagram as illustrated in Figure 9. This contribution is known as the *Schwinger term* and it is common to all three charged leptons. Its value is calculated in Appendix C and the result is

$$a_{\mu}^{\text{QED,LO}} = \frac{\alpha}{2\pi} \approx 1.16 \times 10^{-3}, \quad (30)$$

where α is the fine structure constant that has been measured experimentally in the ^{87}Rb atom with 0.66 ppb precision and has an inverse value of

$$\alpha^{-1}(\text{Rb}) = 137.035\,999\,049(90) \text{ [9]}. \quad (31)$$

Equation (28) can be written to first order in α representing the first-order term in the one-loop diagram contribution

$$g = 2 \left(1 + \frac{1}{2} \frac{\alpha}{\pi} + \mathcal{O} \left(\left(\frac{\alpha}{\pi} \right)^2 \right) \right), \quad (32)$$

where the higher-order corrections to QED processes are suppressed by increasing powers of α . In fact, the QED calculation has been carried out to the fifth-loop contribution

$$a_{\mu}^{\text{QED}} = 116\,584\,71.895 \text{ (0.0009)(0.0019)(0.0007)(0.0077)} \times 10^{-10} \text{ [11]} \quad (33)$$

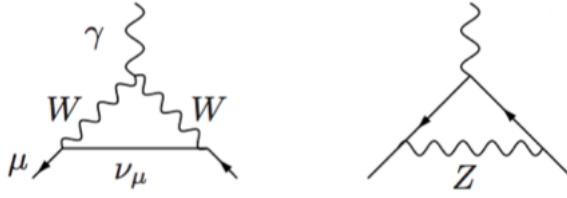


Figure 10: Weak contributions to the muon anomalous magnetic moment: one-loop diagrams with virtual W and Z gauge bosons [10].

with the uncertainties corresponding to the lepton mass ratios, the eighth-order term in the four-loop contribution, the tenth-order term in the five-loop contribution, and the value of the fine structure constant $\alpha(\text{Rb})$. It should be noted that this contribution accounts for over 99.99% of the total contribution to the muon magnetic moment anomaly with much smaller uncertainties than the experimental value.

5.3 The Weak Contribution to a_μ

The weak contribution is the smallest correction to the anomaly. The current electroweak calculation is performed up to two loops. The leading electroweak effect originates from the single loop diagrams of Z and W^\pm bosons shown in Figure 10 with a result of

$$a_\mu^{\text{EW}(1)} = 19.48 \times 10^{-10} \text{ [12]}. \quad (34)$$

The two-loop contribution is negative which reduces the weak contribution, and the third-loop contribution is negligible leading to a total result of

$$a_\mu^{\text{EW}} = 15.36(0.1) \times 10^{-10} \text{ [13]}, \quad (35)$$



Figure 11: The Feynman diagrams for the three different hadronic contributions to a_μ [10].

where the error is due to unknown higher order contributions. Nevertheless, the error is very small. Since the weak contribution to the anomaly is of the order of 1.3 ppm, the 0.54 ppm precision of E821 allowed this experiment to be the first to probe the weak scale of the SM at this precision and subsequently test a_μ^{EW} . Moreover, the value of the EW contribution is smaller than the current discrepancy between experiment and theory which is significant.

5.4 The Hadronic Contribution to a_μ

The hadronic contribution is the second largest contribution, which constitutes about 60 ppm of the total value of a_μ with a dominant error of about 0.4 ppm. This contribution is divided into three pieces: the leading order (LO) and higher order (HO) vacuum polarization (VP) contributions, and the light-by-light (LbL) scattering contribution. Hence, a_μ^{Had} can be expressed as

$$a_\mu^{\text{Had}} = a_\mu^{\text{Had,LOVP}} + a_\mu^{\text{Had,HOVP}} + a_\mu^{\text{LbL}}. \quad (36)$$

Schematics of these three contributions are shown in Figure 11.

VP refers to the partial screening of the charge of a particle by the vacuum which plays the role of a dielectric medium. In the case of the hadronic contri-

680 bution to the muon anomaly, the virtual photon of Figure 9 may lead to the
 681 virtual creation and re-absorption of quark pairs and the corresponding hadrons,
 682 schematically represented in Figure 11 by “had.” corresponding to all possible
 683 hadronic states. While electromagnetic and weak interactions have small values
 684 for their coupling constants allowing perturbative expansions in these constants,
 685 the strong interactions have a small coupling only at high energies preventing the
 686 use of perturbative methods at low energies. Generally, the energy region below 2
 687 GeV cannot be treated using perturbative QCD. The virtual hadrons that affect
 688 the anomaly have an energy scale of $m_\mu c^2 \approx 106$ MeV which is well below the
 689 perturbative QCD region. For this reason, a semi-phenomenological method that
 690 uses experimental input from hadronic e^+e^- annihilation data to evaluate the
 691 LO and HO VP contributions is employed. This method, which makes use of a
 692 dispersion relation, relates the photon VP due to hadronic contributions shown
 693 in the two left diagrams in Figure 11 to the total $e^+e^- \rightarrow$ hadrons cross section
 694 at low energies which is obtained from experimental data. The improvement
 695 in the measurement of e^+e^- annihilation to hadrons at low energies have been
 696 the focus of several experiments. Some of the experiments are CMD2 and SND
 697 collaborations in Novosibirsk (Russia); the KLOE collaboration at Frascati (Italy);
 698 and the BaBar at SLAC (USA). It should be noted that there is an alternative
 699 method in evaluating the VP contributions by using the τ -decays. One of the
 700 most recently reported LO hadronic contribution using e^+e^- -data is

$$a_\mu^{\text{Had,LOVP}} = 694.9(4.3) \times 10^{-10} [5]. \quad (37)$$

701 While the HO hadronic contribution is given by

$$a_{\mu}^{\text{Had,HVP}} = -9.84(0.07) \times 10^{-10} [5]. \quad (38)$$

702 The hadronic LbL contribution, shown in the far right schematic of Figure
 703 11, is of the order of $\mathcal{O}(\alpha_s^3)$ which is quite small. Since the process involves three
 704 virtual photons, the use of experimental data to evaluate the LbL contribution
 705 is not possible. Instead, the contribution is evaluated based on hadronic models
 706 with the requirement that they correctly reproduce the QCD properties. The
 707 downside of this approach is that the final result is model dependent. Currently,
 708 active research work is being done in this area. One of the calculations obtained is

$$a_{\mu}^{\text{Had,LbL}} = 10.5(2.6) \times 10^{-10} [14]. \quad (39)$$

709 5.5 The SM Value of a_{μ}

710 The SM is determined using the QED contribution given in Equation (33)
 711 from [11], the EW contribution given in Equation (35) from [13], the hadronic
 712 LbL contribution given in Equation (39) from [14], the LO VP given in Equation
 713 (37) from [5], and finally the HO VP given in Equation (38) from [5]. The final
 714 result is:

$$a_{\mu}^{SM} = (116\,591\,82.8 \pm 4.5) \times 10^{-10} (0.39 \text{ ppm}) [5]. \quad (40)$$

715 There are several groups that evaluated the anomaly, so the above result is not
 716 the only one. In fact, there is a tension in the theory community related to the
 717 use of τ -data instead of e^+e^- -data to evaluate the LO VP of a_{μ}^{Had} . Except for one

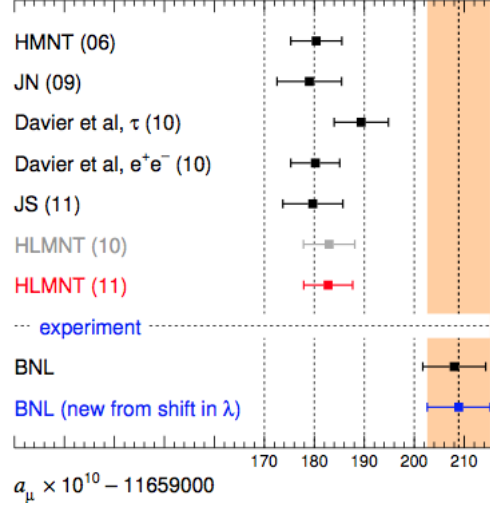


Figure 12: SM predictions of a_μ calculated by several groups. The new experimental result is due to an improvement in the measurement of the muon-to-proton magnetic moment ratio λ [5].

group, all the other evaluations have values close to each other and approximately three standard deviations away from the BNL result as illustrated in Figure 12.

The present error in the SM determination of the anomaly a_μ is dominated by the errors in the LO VP and LbL contributions, 4.3×10^{-10} and 2.6×10^{-10} respectively. The error in the LO VP is expected to diminish to 2.6×10^{-10} by the expected new data from new collaborations such as VEPP-2000 in Novosibirsk and BES-III at BEPC (China). The projected combined error of LO VP and LbL could go down to 3.0×10^{-10} [15]. By combining the proposed Fermilab error of 1.6×10^{-10} with the new expected theoretical error, the total error in the difference between experiment and theory could go down to 3.1×10^{-11} , to be compared with the current 7.7×10^{-11} . By assuming that the experimental and theoretical values of the anomaly do not change, the new deviation is at the 8.1σ

level. This last result is an important motivation for the continuous efforts in improving the experimental and theoretical determinations of the muon magnetic moment anomaly.

6 Conclusions and Prospects

The SM calculation of the anomalous magnetic moment of the muon is smaller than the recent experimental measurement performed by BNL. Depending on the SM evaluation, the discrepancy is approximately $\Delta a_\mu (\text{E821} - \text{SM}) = (25.2 \pm 7.7) \times 10^{-10}$, which is larger than the 3σ level. This difference will be investigated by a future FNAL experiment which aims at reducing the error in the measurement to 1.6×10^{-10} . In parallel, theoretical groups aim at reducing the SM error to 3.0×10^{-10} .

Currently, candidates such as supersymmetry, extra dimensions, and dark matter models attempt to account for the discrepancy. On the high energy frontier, the LHC is sensitive to the electroweak symmetry breaking (EWSB) scale and its extension that may incorporate new particles and new interactions from the above models. While the first run of the LHC has concluded with the discovery of a new particle compatible with the SM Higgs boson, new physics beyond the SM has not yet been found. The new 2015 run of the LHC is expected to collect a significantly large amount of data at $\sqrt{s} = 13$ TeV, and thus probe the weak-scale extensions of the SM. However, even if the LHC discovers new effects, it is still not in its capacity to discern between the possible interpretations of different models.

751 In other words, the LHC data might be compatible with different models leading
752 to alternative explanations. For this reason, the LHC requires complementary
753 experiments to determine the properties of any possible new physics. The muon
754 $g - 2$ is one of the experiments that is sensitive to parameters not accessible to
755 the LHC. The evaluation of the anomaly is affected by a large class of models
756 describing the TeV scale that may be used to constrain the parameter search at
757 the LHC.

758 In short, the muon $g - 2$ magnetic moment anomaly is sensitive to SM physics
759 and beyond which is valuable in complementing searches at the LHC, and at
760 the same time constraining existent and future theoretical models. While the
761 discrepancy between experiment and theory has yet to be confirmed with the new
762 FNAL experiment, and more data at higher energy needs to be collected by the
763 LHC to search for new physics, the muon $g - 2$ remains an important tool to
764 explore physics beyond the standard model at the TeV scale.

References

- [1] F. Jegerlehner, *The Anomalous Magnetic Moment of the Muon* (Springer Berlin Heidelberg, Berlin, 2008).
- [2] J. Beringer et al., Phys.Rev. **D86**, 010001 (2012).
- [3] F. Jegerlehner and A. Nyffeler, arXiv:0902.3360v1 (2009).
- [4] G. W. Bennett et al., Phys. Rev. D **73**, 072003 (2006).
- [5] K. Hagiwara, R. Liao, A. D. Martin, D. Nomura, and T. Teubner, J.Phys. **G38**, 085003 (2011).
- [6] V. Bargmann, L. Michel, and V. Telegdi, Phys.Rev.Lett. **2**, 435 (1959).
- [7] W. Liu et al., Phys. Rev. Lett. **82**, 711 (1999).
- [8] R. Carey et al., FERMILAB-PROPOSAL-0989 (2009).
- [9] R. Bouchendira, P. Clade, S. Guellati-Khelifa, F. Nez, and F. Biraben, Phys. Rev. Lett. **106**, 080801 (2011).
- [10] R. Liao, Ph.D. thesis, University of Liverpool, 2011.
- [11] T. Aoyama, M. Hayakawa, T. Kinoshita, and M. Nio, Phys.Rev.Lett. **109**, 111808 (2012).
- [12] F. Jegerlehner and A. Nyffeler, Phys.Rept. **477**, 1 (2009).
- [13] C. Gnendiger, D. Stckinger, and H. Stckinger-Kim, Phys.Rev. **D88**, 053005 (2013).
- [14] J. Prades, E. de Rafael, and A. Vainshtein, arXiv:0901.0306 (2009).
- [15] T. Blum et al., arXiv:1311.2198 (2013).

⁷⁸⁶ **Appendix A**

⁷⁸⁷ **Spin Dynamics**

⁷⁸⁸ **Appendix B**

⁷⁸⁹ **Muon Decay Rate**

⁷⁹⁰ **Appendix C**

⁷⁹¹ **Radiative Corrections**